



Gas diffusion electrode activity measurements of iridium-based self-supported catalysts produced by alternated physical vapour deposition

Pablo Collantes Jiménez^a, Gustav Sievers^{a, **}, Antje Quade^a, Volker Brüser^a, Rebecca Katharina Pittkowski^{b, ***}, Matthias Arenz^{c, *}

^a Leibniz Institute for Plasma Science and Technology, Felix-Hausdorff-Strasse 2, 17489, Greifswald, Germany

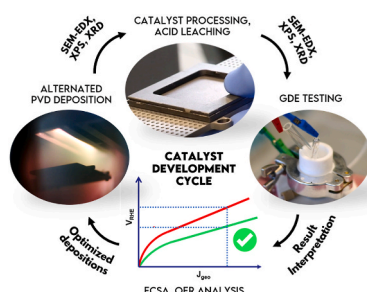
^b Department of Chemistry, University of Copenhagen, Universitetsparken 5, 2100 Copenhagen, Denmark

^c Department of Chemistry, Biochemistry and Pharmaceutical Sciences, University of Bern, Freiestrasse 3, CH-3012, Bern, Switzerland

HIGHLIGHTS

- Electrochemical active surface area and oxygen evolution reaction mass activities scaled with as-deposited Co content.
- Remaining Co suggests a positive effect on the specific activity.
- Accelerated development of oxygen evolution reaction electrode production method and testing demonstrated.

GRAPHICAL ABSTRACT



ARTICLE INFO

Keywords:

PEM Water electrolysis
Oxygen evolution reaction
Physical vapour deposition
Gas diffusion electrodes
Self-supported catalysts

ABSTRACT

The scarce supply of Ir used to catalyze the sluggish oxygen evolution reaction in acidic water electrolysis calls for unconventional approaches to design more active catalysts with minimal resource usage for their commercial scaling. Industrial-ready production methods and laboratory scale tests that can reflect the catalyst behaviour realistically need to be included in this process. In this work, we benchmarked three series of self-supported Ir–Co catalysts with low Ir loading produced by physical vapour deposition under relevant current densities in a gas diffusion electrode setup. It was seen that after selective acid leaching of the Co, a nanoporous structure with a high electrochemically active surface area and a mixed oxide and metallic character was formed. Depending on the initial Co:Ir deposition ratio over ten times higher oxygen evolution mass activities could be reached as compared to a commercial, unsupported IrOx nanoparticle catalyst used as a benchmark in the same setup configuration. The presented integrative catalyst design and testing strategy will help to facilitate bridging the gap between research and application for the early introduction of next-generation catalysts for water splitting.

* Corresponding author.

** Corresponding author.

*** Corresponding author.

E-mail addresses: sievers@inp-greifswald.de (G. Sievers), rebecca.pittkowski@chem.ku.dk (R.K. Pittkowski), matthias.arenz@unibe.ch (M. Arenz).

<https://doi.org/10.1016/j.jpowsour.2023.232990>

Received 22 January 2023; Received in revised form 11 March 2023; Accepted 20 March 2023

Available online 5 April 2023

0378-7753/© 2023 The Authors. Published by Elsevier B.V. This is an open access article under the CC BY license (<http://creativecommons.org/licenses/by/4.0/>).

1. Introduction

Recently, there has been a widespread development of materials and techniques to buffer the intermittent renewable energy supply via diverse applications such as supercapacitors [1–3] and lithium-ion batteries [4,5]. In addition, hydrogen production via proton exchange membrane water electrolysis cells (PEMWEs) stands in the focus of current academic and industrial research. Aside from energy storage for the grid, heat or mobility, PEMWEs can also be a key element in industrial markets that demand hydrogen, such as the ammonia chemical industry, chemical stock synthesis or fuel synthesis (power-to-x) [6]. According to the International Energy Agency (IEA), global demand for hydrogen was estimated at 87 million metric tonnes (MMT) year in 2020 and is forecasted to increase by 13 MM T/year until reaching 528 MMT in 2050 [7]. To reach a net-zero emission scenario in 2050 without further investment in fossil-fuel-based carbon capture, utilization and storage (CCUS) an extra 190 MT of hydrogen power produced by water electrolysis would be necessary to provide 2000 GW of net capacity. To put this development into perspective, by the year 2030 a target for 40 GW in electrolysis capacity should be reached according to the European Green Deal, with an associated cost of EUR 20 to 40 billion without accounting for the electricity costs [8]. While commercial alkaline electrolyzer systems are currently more economical at a lower price per kilowatt [9], PEMWEs have experienced a greater cost reduction due to R&D efforts. The interest in PEMWE development stems from their ability to provide higher current densities and to work at higher temperatures and pressure as compared to alkaline electrolyzers, which makes them a more interesting option for industrial scaling [10]. However, their most challenging limitation is the requirement of Platinum Group Metals (PGMs) such as Ir and Pt to improve the slow electrode reaction kinetics under harsh acidic conditions and high potentials. In particular, the oxygen evolution reaction (OER) occurs in a multi-step reaction that is favoured on the active sites of Ir-based oxide catalysts [11]. While Ru-based oxides have shown higher activity than IrO₂ for the OER, the latter sustains the most balanced equilibrium between high activity and durability in the acidic environment [12]. Since PEMWEs should withstand periods of >50 k operating hours under high current densities and transients without showing significant degradation, the choices are further narrowed. Unfortunately, the supply of Ir and Pt is very limited and costly. Just in the first quarter of 2021, the price per ton of Iridium increased sharply by four times, which is the highest price increase registered in the last 20 years [13]. Hence, to upscale the PEMWE production the capital expenditure (CAPEX) cost including noble metal cost has to decrease. To establish Ir catalysts as a commercially viable and scalable option in PEMWEs, the catalyst loading needs to be reduced while maximizing the catalytic activity. For maintaining a high catalytic activity with low loadings, the electrochemically active surface area (ECSA) should be as high as possible. A common strategy to reduce the catalyst loading is to develop alloys with synergistic effects that increase the intrinsic activity [14] as is observed when combining Ir with Cu, Co, or Ni [15,16] or forming core-shell structures [17] that benefit from an Ir-rich surface [18–20]. Another approach is to develop completely PGM-free catalysts based on alloys of more abundant metals, i.e., Co, Ni, Fe or Mo derived from metal-organic frameworks (MOF) [21–24]. However, the most known commercial catalysts are still unsupported, Ir-based nanoparticles. Several synthesis approaches have been tested to produce nanoparticles with different characteristics [25]. It is not possible to support the nanoparticles on carbon to increase the surface area, as the carbon degrades. This has the disadvantage that the ECSA of Iridium black is small compared to Pt/C catalysts used in fuel cell systems [11,26–28]. Recently developed self-supported catalyst nanostructured catalysts present a possible solution to this problem since the catalyst is applied on the substrate (e.g., a gas diffusion electrode) directly without using binder materials. With this approach, it already has been shown that microstructure tuning and modulation of the catalysts' electronic structure with heteroatoms can

produce highly active and stable catalysts [29–32]. However, multi-step processes are often used at the lab scale to synthesize catalyst particles and coatings, which can impose limitations in the industrial scaling. On the other hand, physical vapour deposition (PVD) is a well-known technique in the industry. The plasma process yields homogenous composition in the layers and allows flexible operative conditions such as the direct deposition of oxides or control of the morphology modifying, e.g., the sputtering angle or chamber pressure [33]. In recent studies, PVD has been used to produce highly active self-supported catalysts with tunable morphologies using a co-sputtered templating metal [11,34,35]. High ECSAs are achieved by selective dissolution of the templating metal in an acid-leaching processing step, which creates an interconnected network of the active metal. Several publications concerning this method report large ECSAs and activities [11,34,35]. On the other hand, the high catalyst performance observed with traditional academic testing techniques such as the thin-film rotating disk electrode (TF-RDE) hardly ever translates to real operation conditions seen on full membrane electrode assembly (MEA) systems [36]. The step from lab testing to an industrial application is thus very wide. Testing in a liquid acidic environment under mass transport limited conditions does not describe accurately those of a Membrane-Electrode-Assembly. Furthermore, it has been discussed that the degradation trials on OER could have been systematically misinterpreted [37–40]. Due to the method limitations, the oxygen evolved during the reaction is trapped close to the surface of the catalyst causing early failure during the test, while the catalyst features remain unchanged [39]. Gas diffusion electrode (GDE) setups have been introduced as a bridging tool as they include realistic constraints (real catalyst loadings, membrane layer, gas diffusion/porous transport layers, three-phase boundary) while keeping the fast screening capabilities of the TF-RDE and retaining the ability to measure the potential drop of the anode in a three-electrode setup. While initially designed for oxygen reduction reaction (ORR) studies [41–43], an increasing number of publications with GDE setups in different configurations also prove its flexibility to explore different reactions such as the OER [25]. It is expected that this technique becomes a standard in the electrochemical community and is used more systematically to develop catalyst layers in a fast and cost-effective manner before applying MEA tests [44]. In the present study, we use a GDE setup modified to accommodate electrolysis conditions to perform an electrochemical characterization of the OER in three series of IrCo catalysts produced by PVD with different sputtering Co:Ir ratios. In particular, we aim to study the influence of the deposition parameters on the reaction performance. To that end, we use morphological and chemical characterization techniques (SEM-EDS, XAS, XRD, XPS) to follow the development of the catalyst during different steps in the material preparation (magnetron sputtering followed by acid leaching). The features observed (mesoporosity, chemical distribution, crystallinity) are further discussed alongside the electrochemical characterization of the ECSA of the catalyst by cyclic voltammetry (CV) and OER mass activity. Our findings indicate a direct relationship between the deposition parameters and the electrochemical results. Furthermore, this study underlines the interesting synergy of the PVD with the GDE method to fast-track catalyst film optimization for industrial applications.

2. Experimental section

2.1. Materials, chemicals, gases

De-ionized ultrapure water (resistivity >18.2 MΩ cm, total organic carbon (TOC) < 5 ppb) from an Aquinity P –10² system (Membrapure, Germany) was used for electrolyte preparation and the cleaning of the GDE half-cell. Carbon gas diffusion layers (GDL) with a microporous layer (MPL) (Sigracet 29BCE, 325 μm thick, Fuel Cell Store) served as a substrate for the sputtering of the catalyst film. A polytetrafluoroethylene (PTFE) disk (Bola, 0.12 mm thickness), a GDL without an MPL

(Freudenberg H23, 210 μm thick, Fuel Cell Store), a porous transport layer (PTL) (ANKURO Int. GmbH, 0.3 mm thickness, 50% open porosity), and a Nafion membrane (Nafion 117, 183 μm thick, Chemours, Wilmington, DE, USA) were used for the cell assembly (see Fig. 1). As a counter electrode (CE) a platinum wire of 0.5 mm diameter (99.99%, Junker Edelmetalle GmbH) was used, which was folded several times at one side to increase the active surface area. Another Pt wire was used to manufacture a hydrogen reference electrode (RE) using a borosilicate glass capillary of 40 mm in length and 6 mm in diameter. Additionally, self-manufactured borosilicate glass frits (6 mm internal diameter, 20 mm length) were used to hold the RE during the electrochemical measurements. Perchloric acid (70% HClO_4 , Suprapur, Merck) was used for electrolyte preparation. O_2 (99.999%, Air Liquide) and Ar (99.999%, Air Liquide) were used for magnetron sputtering, acid leaching, and electrochemical measurements.

2.2. Catalyst synthesis - preparation of the Ir-Co network

To prepare the self-supported nanoporous catalyst film, a linear sputtering magnetron reactor (Univex 400, Leybold GmbH, Germany) was used. The process chamber was evacuated to a pressure of $1.7 \cdot 10^{-5}$ Pa. The film substrate (GDL) was placed on a holder in a load lock at atmospheric pressure and then evacuated to a base pressure of at least 10^{-4} Pa. From there, a swivelling arm allowed the holder to enter the process chamber with minimal interruption. During the deposition, an Ar plasma was ignited at the magnetron electrode at a working pressure of 5 Pa and flushed through the individual magnetron sources at a flow rate of 100 sccm. For the $\text{Ir}_x\text{Co}_{1-x}$ film deposition, two magnetrons were equipped with planar targets of Co (99.95%, Evotec GmbH, Germany) and Ir (99.95%, MaTeck, Germany) of $177 \times 25 \times 1.5$ mm located at the upper part of the chamber. The RF generators (Cito 136, COMET) operated at a driving frequency of 13.56 MHz. Further information about the sample preparation process and the reactor configuration can be found in the SI. A mask of $5 \text{ cm} \times 5 \text{ cm}$ on the substrate holder limited the sputtered area during the deposition. The sample was allowed to oscillate in a linear trajectory between the two respective magnetrons. The sputtering was initiated when the sample reached the position below each magnetron. At that point, the sample holder was programmed to oscillate with an amplitude of 1 mm to increase the homogeneity of the deposition. The holder reached an acceleration of 100 mm s^{-2} and a maximum linear velocity of 50 mm s^{-1} . The RF power was chosen as 225 W for Co and 50 W for Ir. The alternating sputtering process was performed for 500 cycles in all series, modifying the deposition time to achieve three different element ratios as seen in Table 1. The average deposition time was 4–5 h. Before the

Table 1

Material parameters during the magnetron sputtering process.

Series By element wt.% (EDX)	Sputtering time (s)	Number of cycles	Loading Ir ^a (mg cm^{-2})	Gas atmosphere	Substrate type
$\text{Ir}_{28}\text{Co}_{72}$	Ir: 3 Co: 6	500	0.250	Ar 100%	GDL 29BCE
$\text{Ir}_{45}\text{Co}_{55}$	Ir: 3 Co: 3	500	0.250	Ar 100%	GDL 29BCE
$\text{Ir}_{75}\text{Co}_{25}$	Ir: 3 Co: 1	500	0.250	Ar 100%	GDL 29BCE

^a Theoretical loading calculated by mass gravimetry.

measurements, a calibration of the sputtering process was performed where Ir was sputtered continuously for 20 min on a substrate. The final Ir loading was measured by mass gravimetry, and the thickness homogeneity was verified using a profilometer (Alpha Step D-600, KLA). Assuming a linear dependency of loading with the sputtering time, three series were produced with a nominal Ir loading of 0.250 mg cm^{-2} and different Co:Ir deposition time ratios. The resulting Co:Ir ratios were determined experimentally by EDX on the as-prepared samples (Table 1).

As part of the Ir-Co catalyst film preparation, the samples were leached after the deposition in 1 M HClO_4 to create a nanoporous self-supported Ir structure by selectively dissolving the Co under potential-controlled conditions according to the method developed by Sievers et al. [11]. The individual steps of the acid leaching procedure are summarized in Table 2 and described more in detail within the Result and Discussion section. Once the samples were leached, they were cleaned in distilled water and left to dry in air before further manipulation.

2.3. Gas diffusion electrode setup

The GDE was prepared using a Nafion membrane (Nafion 117, 183 μm thick, Fuel Cell Store) hot pressed to the sputtered gas diffusion layer (GDL). In this study, the Nafion membrane was activated as described by Schröder et al. [25]. A concentric circular steel punch (BOEHM, Germany) was used to cut small disks from the GDL and the assembly material. First, a disk of $\varnothing 3 \text{ mm}$ was cut from the sputtered GDL. Using an in-house built hot press (Fig. S1) with a modified soldering iron and 6 kg steel weights, a $\varnothing 10 \text{ mm}$ Nafion membrane was hot pressed on top of the catalyst layer at 120°C using 84 kg cm^{-2} for 30 s.

As indicated in Fig. 1, a $\varnothing 20 \text{ mm}$ Gas Diffusion Layer (GDL) without

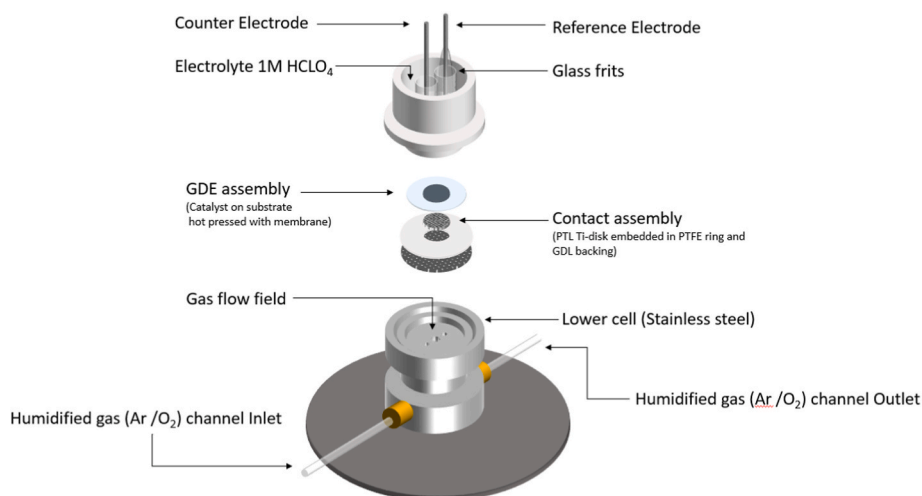


Fig. 1. GDE half-cell setup used in the study and assembly view of all elements.

Table 2

Electrochemical protocol for OER activity trials.

Acid leaching	Cyclic Voltammetry (CV)	Activation (Potentiostatic)	OER (Galvanostatic)	Steps	
30 cycles	30 cycles	20 min	30/60 °C	Step 0	Leaching
100 sccm Ar	100 sccm Ar	100 sccm Ar	100 sccm O ₂	Step 1	1. CVs (ECSA)
100 ml 1 M HClO ₄	4 ml 1 M HClO ₄	4 ml 1 M HClO ₄	4 ml 1 M HClO ₄		2. OER 30 °C
0.05–0.5 V _{RHE}	0.05–1.2 V _{RHE}	1.7 V _{RHE}	1 - 1000 Ag ⁻¹	Step 2	3. CVs
100 mVs ⁻¹	100 mVs ⁻¹	Online iR-comp.	5 min/step		1. CVs
5 kHz, 5 mV AC	5 kHz, 5 mV AC		Post iR correction	Step 3	2. Act.
	Post iR correction				3. CVs
					4. OER 30 °C
					5. CVs
					1. OER 60 °C
					2. CVs

a microporous layer (MPL) was placed directly over the flow field of the stainless-steel bottom cell. On top, a Ø 20 mm Teflon disk with a Ø 3 mm center hole was used as a sealant for the liquid and electrical insulator. Embedded inside, a Ø 3 mm PTL disk was positioned to allow the gas flow to contact the GDE on top and to serve as a current collector. Last, a Teflon upper cell was pressed against the assembly and secured tightly with a metal clamp. Both the Teflon upper cells and the CE and RE were cleaned before every use according to the following protocol. First, they were placed overnight in a tank with concentrated HNO₃ and concentrated H₂SO₄ solution 1:1 in volume. Afterwards, they were rinsed and boiled in distilled water for 1 h in at least 5 cycles. The unused materials were kept in a glass vial and boiled always one last time before use. Furthermore, the Pt wire was flame annealed every time it was used to remove any organic contaminations. After every trial, all the assembly components were discarded and replaced with new ones to decrease the influence of contaminations.

2.4. Electrochemical measurements

All the experiments were conducted with a Potentiostat (ECi-211, Nordic Electrochemistry ApS, Denmark). The Potentiostat also controlled the gas switching between humidified Ar and O₂ during the experiments. An overview of the experimental protocol is presented below in Table 2.

The GDE half-cell (Fig. 1) and a glass bubbler were placed inside an insulating glass chamber during the measurements (See Fig. S1 in SI). Precise temperature control (± 0.1 °C) was achieved through a constant flow of distilled water recirculated in between the double glass walls with a water heating system (Lauda RC6 SC). The GDE half-cell was placed in the middle of the chamber, supported on an aluminium laboratory jack (Laborboy, Sigma Aldrich) and insulated with a PTFE plate in between. Before the start of the measurements, the system was allowed to equilibrate at a constant temperature for at least 30 min. All the temperature references correspond to the set point defined in the water heating system. To prevent any shifts in reference potential due to contaminations on the RHE electrode, the RE was protected in a glass frit manufactured by an in-house technical glassblower. In addition, the RHE electrode was calibrated before each measurement in a separate GDE cell against a Pt GDE with the same molarity and electrolyte as the testing GDE cell, i.e., 1 M HClO₄ electrolyte. The H₂ gas was supplied

through an in-house electrolyzer, connected to the gas flow through lines of the GDE cell. The RHE offset was measured by cyclic voltammetry in a potential interval between -0.005 and 0.005 V at 100 mV s⁻¹ for 200 cycles. The acceptable range for initial RHE values was defined as ± 0.003 V_{RHE}. In case of a larger deviation, the RHE was remade, and the calibration procedure was repeated to avoid large iR-correction errors. Before the measurements, Ar was purged through the flow field as a conditioning step and cyclic voltammograms were recorded at a scan rate of 100 mV s⁻¹ in a potential range between 0.025 and 1.2 V_{RHE} until a stable cyclic voltammogram could be observed (ca. 30 cycles). The ECSA of the catalyst (Table 3) was determined by integrating the H_{upd} area in the potential window of 0.025 – 0.25 V_{RHE} of the last CV acquired using a fixed conversion coefficient of 176 μ C cm⁻² [11] according to the following formula:

$$ECSA [m^2 g^{-1}] = \frac{QH_{upd}}{L_{ir} \times 176 \mu C cm^{-2}} \quad (1)$$

The OER activity was determined through a galvanostatic step protocol with increasing currents based on Schröder et al. [25] and scaled accordingly to account for the loading difference. An AC signal (5 kHz, 5 mV) was applied during the current steps to obtain an online resistance measurement between the working and reference electrode (~ 10 Ω) which was used for an iR-correction of the measured potential values.

3. Results & discussion

3.1. Catalyst morphology and chemical composition

The morphology of the unleached catalyst layers, i.e., after the deposition process, was characterized using secondary electron imaging (SEM), see Fig. 2. As seen in Fig. 2a, b and c, all catalyst series featured a similarly packed globular structure. Similar morphologies have been previously observed in studies of catalyst films prepared on carbon paper substrates using comparable process conditions [33]. The size of the globular features was not substantially different between the respective series, ranging from 0.1 to 0.9 μ m in diameter. However, the SEM micrographs indicate further development of nanoporous structures. That is, the surface of the globules exhibits a certain degree of roughness, which is especially distinct for the Co-rich series (Ir₂₈Co₇₂; in the following the notation refers to the elemental composition obtained

Table 3

Relevant electrochemical parameters for the catalyst series included in the study. Error measurements are expressed from the average of three trials per series.

Series By element wt. %	Tafel slope (mV dec ⁻¹) @30–100 Ag ⁻¹ _{ir}		Mean ECSA (m ² g ⁻¹) A _{geo} = 0.0707 cm ² C = 176 μ Ccm ⁻²	Mass Activity (Ag ⁻¹)		Specific Activity (Am ⁻²)	
	Activated 30 °C	60 °C		@1.50 V _{RHE} Activated 30 °C	@1.46 V _{RHE} 60 °C	@1.50 V _{RHE} Activated 30 °C	@1.46 V _{RHE} 60 °C
Ir ₂₈ Co ₇₂	62	49	52.6 \pm 4.8	101.5	117.8	1.9	2.2
Ir ₄₅ Co ₅₅	64	52	33.7 \pm 1.9	57.6	91.8	1.7	2.7
Ir ₇₅ Co ₂₅	68	58	21.4 \pm 2.0	44.3	62.7	2.1	2.9
Alfa Aesar	53	47	–	12.14	10.18	–	–

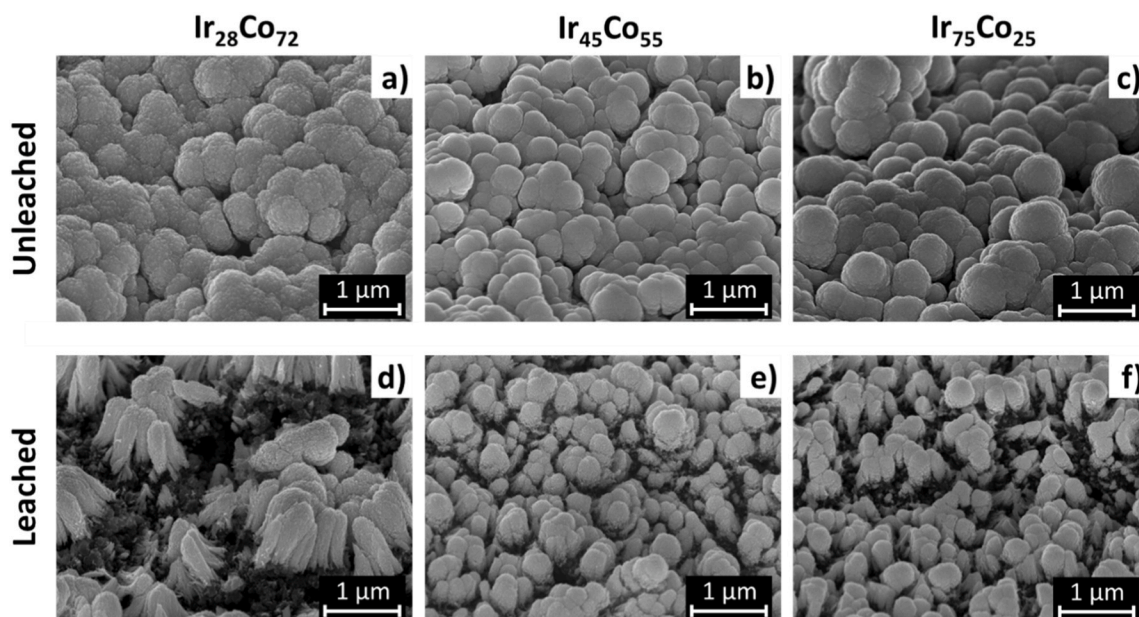


Fig. 2. SEM SE top measurements of IrCo catalysts on a carbon substrate taken with a 45° angle from the surface, at 15 kV and 10 k magnification. a) to c) correspond to the samples before the electrochemical dealloying in HClO_4 1 M for 30 cycles between 0.05 and 0.5 V_{RHE} while d) to f) show the surface of the same samples after the process. A summary of EDX results normalized for Ir and Co is expressed in weight % (upper table) and atomic % (lower table). The results were obtained at 15 kV, averaged from 5 spots across the image area.

by EDX point analysis before the acid leaching), see Fig. 2a as well Fig. S2b for a closer look. Finally, yet importantly, EDX top-down mapping of different representative areas on the catalyst films, see Fig. S3, revealed that in all cases Ir and Co were homogeneously distributed across the film. As mentioned before in the Method section, Co was removed from the sputtered films in a process that is referred to as acid leaching. As the Pourbaix diagrams show for the respective catalyst film constituents, metallic Ir is stable under the leaching conditions while Co is oxidized to soluble Co^{2+} ions and does not form a passive film [45,46]. Hence, Co dissolution starts spontaneously when a sputtered sample is submerged in a de-aerated 1 M HClO_4 aqueous solution [11], giving the solution had a characteristic pink tone. The color of this solution has been described extensively as a result of the complexation of Co^{2+} complex in water to form $[\text{Co}(\text{H}_2\text{O})_6]^{2+}$. To confirm this, Cl^- ions were added to the solution from concentrated HCl and the temperature was raised. Both effects shift the equilibrium to $[\text{CoCl}_4]^{2-}$ as a direct consequence of Le Chatelier principle [47], which shows a distinct blue color, see Fig. S4. To attain better control of the acid leaching process and to minimize Ir oxidation before ECSA determination of the metallic surface, the samples were submitted to an electrochemical cycling protocol (Table 2) between 0.05 V_{RHE} and 0.5 V_{RHE} with a scan rate of 100 mV s^{-1} starting directly after the electrolyte was added to the upper cell compartment. The cycling continued until a stable CV was achieved. This was typically the case after 30 potential cycles. Along this process, the initial Co to Ir ratios were changed significantly. In every case, the relative amount of Co decreased to under 10% in weight according to the EDX. Using XPS for a more surface-sensitive analysis of the pre-leached and leached samples, see Fig. S5, we observed a trend in the decrease in the Co:Ir ratios after leaching following the series, albeit not proportional to the initial ratios (see Fig. S6). This discrepancy could perhaps be attributed to the drastic change in morphological differences and chemical gradients to form a more stable Ir shell with a Co core after the acid leaching [11,47,48]. The process of acid leaching has been well described for Pt-based alloys for the oxygen reduction reaction. It has been shown by low energy ion scattering (LEIS) that the exposition of PtM ($M = \text{Fe}, \text{Co}, \text{Ni}$, etc.) surfaces automatically leads to a full depletion of all non-noble atoms from the surface and the formation of “skeleton” or core shell surfaces [48]. In

the here reported work, sparse colonies of Ir-rich dendritical structures were formed of the GDL carbon substrate, which was also left exposed over large areas. The development of this porous structure differs substantially from the preparations on glassy carbon in a former study [11], see Fig. S2. The reason for this difference might be the three-dimensional structure of the gas diffusion electrode or the hydrophobicity. The initially Co-rich sample, $\text{Ir}_{28}\text{Co}_{72}$ presents the biggest size of the dendrites and area of the exposed substrate. Both features appeared to decrease together with the Co:Ir ratio when comparing $\text{Ir}_{28}\text{Co}_{72}$ with the $\text{Ir}_{45}\text{Co}_{55}$ and $\text{Ir}_{75}\text{Co}_{25}$ series (Fig. 2d, e and f respectively).

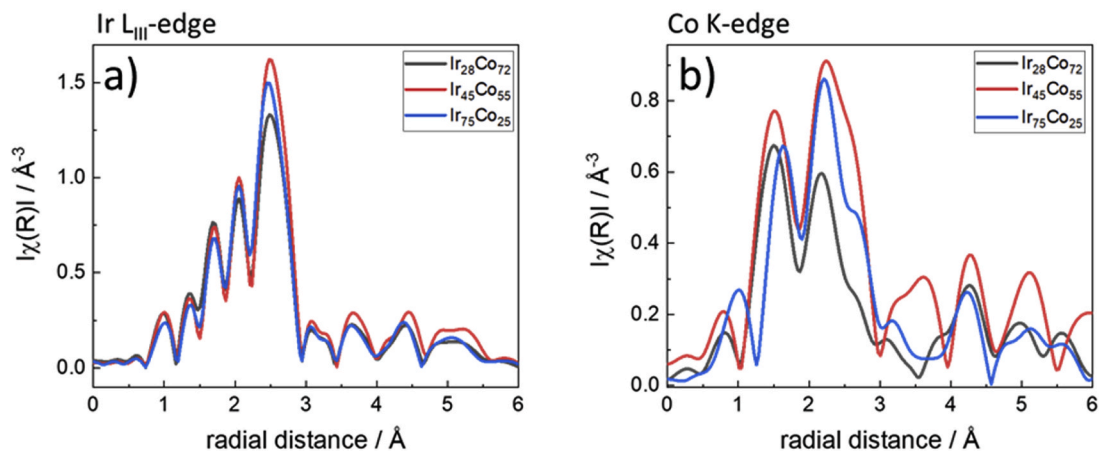
Series By element wt.%	wt.% norm.			
	Unleached		Leached	
	Ir	Co	Ir	Co
$\text{Ir}_{28}\text{Co}_{72}$	27.7 ± 1.9	72.3 ± 1.9	95.0 ± 0.8	5.0 ± 0.8
$\text{Ir}_{45}\text{Co}_{55}$	44.9 ± 0.7	55.1 ± 0.7	96.2 ± 1.5	3.8 ± 1.5
$\text{Ir}_{75}\text{Co}_{25}$	75.3 ± 5.1	24.7 ± 5.1	91.9 ± 0.8	8.1 ± 0.8
Series By element at.%	at.% norm.			
	Unleached		Leached	
	Ir	Co	Ir	Co
$\text{Ir}_{28}\text{Co}_{72}$	10.5 ± 0.9	89.5 ± 0.9	85.4 ± 2.1	14.6 ± 2.1
$\text{Ir}_{45}\text{Co}_{55}$	19.8 ± 0.7	80.2 ± 0.7	88.6 ± 4.1	11.4 ± 4.1
$\text{Ir}_{75}\text{Co}_{25}$	48.8 ± 6.7	51.3 ± 6.7	77.8 ± 1.9	22.2 ± 1.9

The element distribution of representative leached areas can be found in the EDX mapping of Fig. S3 of the SI. An as-sputtered XRD analysis indicated that the elements are found in a heterogeneous film with a low degree of crystallinity, as it is normal for sputtered catalysts that do not experience a heat treatment [26,49,50]. While the overall structure remains amorphous, the shift to lower theta values and narrowing of the Ir (111) Bragg peak after leaching, see Fig. S7, suggests that it might experience a slight increase in crystallinity, which has also been reported in similar studies [11,34,51]. Since the first studies on AuAg nanoporous structure formations via selective leaching, several studies have emerged to explain the behaviour of homogeneous bimetallic alloys [52–57] as well as the change in electronic properties due to the formation of core-shell nanoparticles. However, a former study using a similar magnetron-sputtering and acid-leaching process to create a

self-supported Pt–CoO network revealed that no alloy was formed in the bimetallic deposition or leaching process [35]. A further look into the oxidation state and the small range structures of the Ir–Co series was conducted by ex-situ X-ray Absorption Spectroscopy (XAS) of the leached samples, see Fig. 3 and Figs. S8–10 of the SI. Data were collected at both, the Co and Ir edge, however, due to the low Co content the data quality is significantly lower for the Co edge than for the Ir edge. Therefore, we draw our conclusions mainly from the data obtained from the Ir L_{III} K-edge. The X-ray absorption fine structure (EXAFS) results reveal mixed metallic and oxide structures, see Fig. 3. The presence of Co–Co₁ and Ir–Ir₁ coordination indicates that a proportion of Co and Ir remains metallic after acid leaching and exposure to air. Furthermore, the presence of Ir–Co₁ coordination shows a partial alloy character with a similar trend as observed in the Co content of the leached samples by

EDX: Ir₇₅Co₂₅ > Ir₂₈Co₇₂ > Ir₄₅Co₅₅. In addition, Ir–O₁ and Co–O₁ coordination is seen indicating partial oxidation of the samples. Interestingly, the data from all series indicate a similar Ir–O₁ bond length, indicating that the Co content has no measurable effect on lattice strain.

Considering the mixed chemical nature of the material, we describe it as Ir_xCo_{1-x} nanoclusters rather than an IrCo alloy. In this context, the self-supported structure is achieved by the dissolution of a sacrificial templating metal in a selective acid leaching process under potential conditions, coupled with surface restructuring processes in the material due to diffusive forces. In an earlier study from the same authors concerning the leaching behaviour of co-sputtered noble and non-noble metals in a Pt–Cu system, a mechanism of acid leaching process leading to self-supported nanostructured catalysts was already discussed [34]. As the non-noble metal dissolves in acid, hydrogen gas evolution



Co-edge

Sample	bond	N	R / Å	$\sigma^2 / \text{\AA}^2$	E ₀ / eV	R _f
Ir ₂₈ Co ₇₂	Co–O ₁	1.9 ± 0.7	1.94(5)	0.003	7712 ± 9	0.037
	Co–Co ₁	1.2 ± 1.0	2.58(5)	0.004(8)		
	Co–Ir ₁	3.2 ± 2.3	2.60(8)	0.012		
Ir ₄₅ Co ₅₅	Co–O ₁	2.1 ± 0.5	1.91(3)	0.003	7711 ± 6	0.018
	Co–Co ₁	1.1 ± 0.9	2.54(8)	0.004(6)		
	Co–Ir ₁	4.3 ± 0.9	2.64(2)	0.010		
Ir ₇₅ Co ₂₅	Co–O ₁	1.2 ± 0.6	1.98(4)	0.003	7718 ± 6	0.014
	Co–Co ₁	2.0 ± 1.3	2.66(6)	0.004(5)		
	Co–Ir ₁	3.4 ± 1.2	2.64(2)	0.010		

Ir-edge

Sample	bond	N	R / Å	$\sigma^2 / \text{\AA}^2$	E ₀ / eV	R _f
Ir ₂₈ Co ₇₂	Ir–O ₁	1.3 ± 0.3	1.99(2)	0.003(3)	11224 ± 2	0.019
	Ir–Co ₁	1.4 ± 0.9	2.63(6)	0.012(9)		
	Ir–Ir ₁	6.7 ± 1.7	2.68(1)	0.005(1)		
Ir ₄₅ Co ₅₅	Ir–O ₁	1.0 ± 0.4	1.99(3)	0.003(1)	11223 ± 2	0.026
	Ir–Co ₁	0.7 ± 0.5	2.64(7)	0.010(4)		
	Ir–Ir ₁	8.2 ± 0.4	2.68(1)	0.005(1)		
Ir ₇₅ Co ₂₅	Ir–O ₁	1.0 ± 0.2	1.99(3)	0.003(3)	11225 ± 2	0.007
	Ir–Co ₁	1.9 ± 0.7	2.63(3)	0.010(5)		
	Ir–Ir ₁	6.7 ± 1.1	2.67(1)	0.005(1)		

Fig. 3. Fourier transformed magnitudes of the k^2 weighted extended X-ray absorption fine structure (EXAFS) data of the leached Ir_xCo_y samples, shown for the a) Ir L_{III}-edge and the b) Co K-edge.

starts spontaneously. Some of the gas can be trapped in interior cavities and mechanically push the material around to nucleate pores. At the same time, the catalyst-rich areas undergo a surface diffusion process due to the electrochemical and mechanical forces, which promote the redeposition of catalysts in neighbouring regions. The structures created in such a process depend on the irregularities of the morphology and porosity at the surface. Surface diffusion of catalyst particles is evidenced by an Ir enrichment and depletion of Co over the surface observed in the EDX maps (Fig. S3) and reinforced by the XPS results (Fig. S6). This process would be in agreement with the different morphologies observed in the series between the as-deposited and leached state for the different EDX Co:Ir ratios and the different initial distributions of Ir and Co-rich areas. A previous study of a very similar Ir–Co catalyst already demonstrated that Co dissolves from all areas in contact with the acid solution leaving a percolated Ir network with the same domain size as the initial deposition [11], which corresponds well with the results presented here.

3.2. GDE electrochemical characterization and activity measurements

After sputtering and acid leaching, each series of the catalyst layers was assembled into the GDE setup for electrochemical testing. The aim

of the electrochemical testing was twofold: first, the electrochemically active surface area (ECSA) of the leached Ir was determined. This was achieved by determining the H_{upd} area in cyclic voltammetry [58]. The leaching conditions were designed to dissolve the Co while preserving Ir in metallic state, as IrO_2 does not display any H_{upd} area. We assume that after leaching any oxidized Ir surface would be reduced and that there is a direct relationship between metallic Ir surface before activation and ECSA after activation. The second aim was to activate the catalyst layer and determine its activity for the OER.

The electrochemical characterization is exemplified in Fig. 4a which depicts the CV and OER activity of a leached Ir-rich ($\text{Ir}_{28}\text{Co}_{72}$) nano-structured IrCo film. It is seen that after leaching, the CV displays a pronounced H_{upd} area indicative of metallic Ir, allowing a straightforward ECSA determination of $52.6 \pm 4.8 \text{ m}^2\text{g}^{-1}$, Fig. 4a. After recording the CV, the gas was switched, and oxygen was flushed through the cell at 1 sccm for 20 min to guarantee a saturated oxygen atmosphere. The OER activity was determined before and after activation and benchmarked to published data from a commercial IrO_2 black powder (Alfa Aesar) [25]. It is worth mentioning that the commercial sample was prepared with a different loading (1 mg cm^{-2}) than the samples in this study. However, it is still considered to be a useful reference since the OER activities were measured using the same protocol and setup

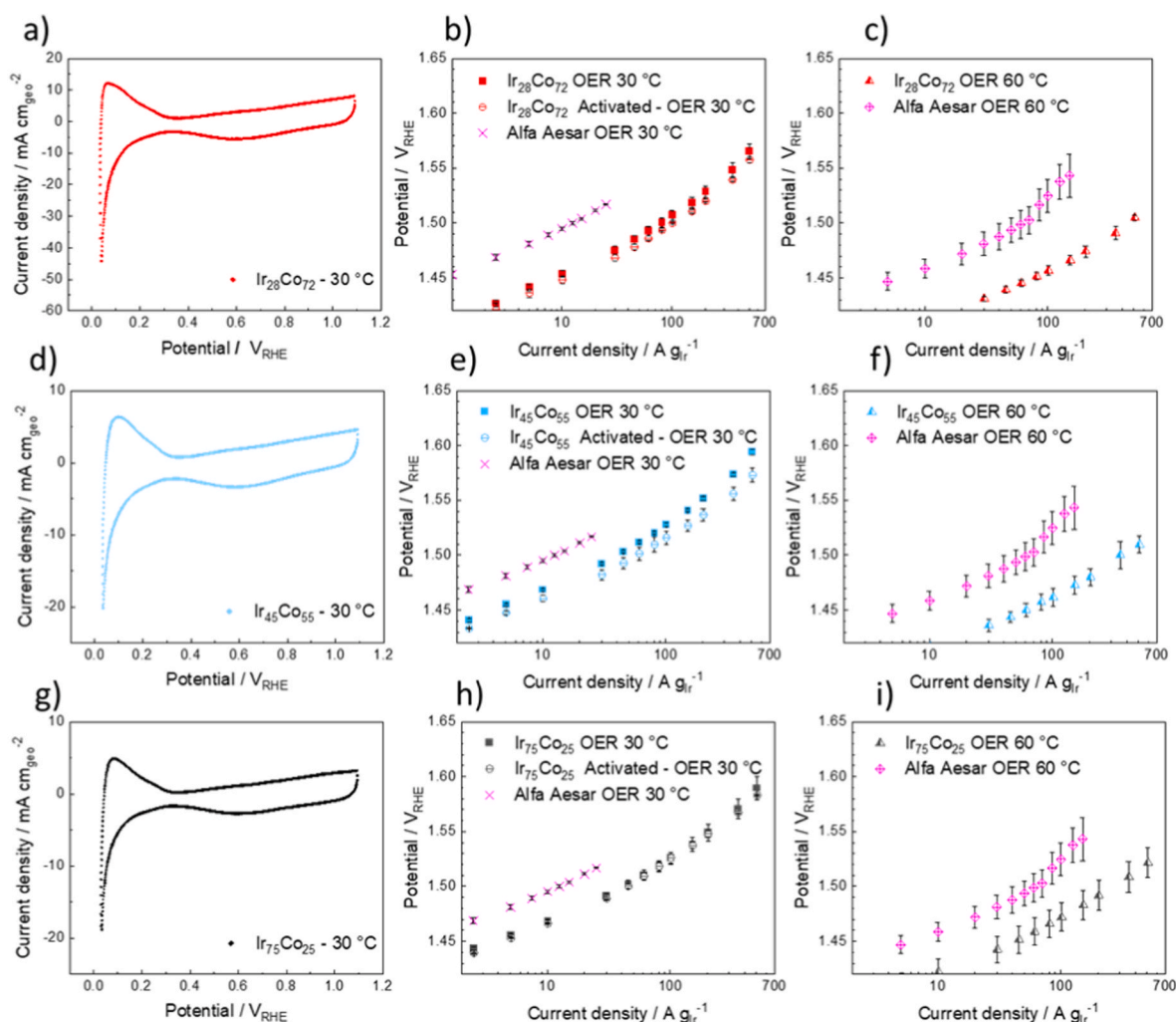


Fig. 4. Average of three cyclic voltammograms in Ar atmosphere measured at 30 °C, 100 mVs^{-1} in 1 M HClO_4 for the a) $\text{Ir}_{28}\text{Co}_{72}$, d) $\text{Ir}_{45}\text{Co}_{55}$ and g) $\text{Ir}_{75}\text{Co}_{25}$ series with a common iridium loading of $250 \mu\text{g}/\text{cm}^2$ before leaching (Table 1). iR-corrected OER mass activity in 100% humidified oxygen at 30 °C measured over the last 10 s of each 300-s current step from the commercial sample and b) $\text{Ir}_{28}\text{Co}_{72}$, e) $\text{Ir}_{45}\text{Co}_{55}$ and h) $\text{Ir}_{75}\text{Co}_{25}$ series in as-prepared (filled symbols) and activated (hollow symbols) states. iR-corrected OER mass activity in 100% humidified oxygen at 60 °C measured over the last 10 s of each 300-s current step for the commercial sample and c) $\text{Ir}_{28}\text{Co}_{72}$, f) $\text{Ir}_{45}\text{Co}_{55}$ and i) $\text{Ir}_{75}\text{Co}_{25}$ series. Each individual data point and error bars represents respectively the average and standard deviation of three different sample measurements.

configuration. The first set of OER activities revealed that the catalyst surface was not yet completely activated into IrO_x . Yet, the OER overpotential in this state was around 40 mV lower as compared to the benchmark. Recording another set of CVs in Ar atmosphere after the first OER measurements confirmed that remainders of metallic Ir were present from a decreased but still discernible H_{upd} area. In addition to the reduced H_{upd} area, the double-layer capacity was increased (Fig. S11b). To complete the oxidation of the metallic Ir, a potentiostatic activation step was applied at 1.70 V_{RHE} for 20 min in O_2 atmosphere (Fig. S12), after which a second set of OER activities was recorded. The fact that the overpotential was reduced by an additional 10 mV as compared to before activation indicates the further formation of the active IrO_2 phase. Nevertheless, recording another set of CVs in Ar atmosphere in step 2.3 of the protocol (Table 2) shows that a complete, irreversible oxidation of the surface has not yet been achieved and still some H_{upd} area is visible (Fig. S11c). Despite the incomplete activation, the OER mass activity at 1.50 V_{RHE} was 101.5 $\text{Ag}^{-1}_{\text{Ir}}$, roughly eight times higher than that of the commercial benchmark catalyst Table 3). In the third and last step of the protocol the temperature was increased from 30 to 60 °C and OER activity was determined for one last time (Fig. 4c). The raise in temperature leads to a clear decrease in overpotential of ca. 40 mV even at the lowest (20 $\text{Ag}^{-1}_{\text{Ir}}$) current densities (Fig. S13). At this temperature, an OER activity of 117.8 $\text{Ag}^{-1}_{\text{Ir}}$ was determined at 1.46 V_{RHE} . Interestingly, in addition to a temperature-induced kinetic activation, the raise in temperature leads to an additional activation via further oxidation. This can be seen by the fact that the relative OER mass activity increases to a threefold value. In comparison, the benchmark catalyst is mostly oxidized in its initial state. A further description of the contributions to the decreased overpotential due to temperature and activation contributions can be found in the SI. In addition to the activation, it is seen that with the temperature rise the Tafel slope decreased slightly from 62 to 49 mV dec^{-1} . This is a small, but still, significant change, which can be explained by the temperature dependency of each rate constant for every step of the reaction according to Arrhenius' equation [59]. The electrochemical response of the $\text{Ir}_{45}\text{Co}_{55}$ series presented in Fig. 4d–f shows a similar development as the former discussed Co-rich series. From the initial CVs after acid leaching the measured H_{upd} region after acid leaching was determined to be $33.7 \pm 1.9 \text{ m}^2\text{g}^{-1}$. A possible explanation for the decreased surface area could be a smaller size of the features formed after the Co leaching (Fig. 2e) and less internal porosity. Since the measured surface area at the initial step (Fig. S11a) was only around half of the Co-rich series (Fig. 2a), the oxide formation after the activation in Step 2.3 (Table 2) also rendered a smaller oxide capacitive layer (Fig. S11d). However, at this point the $\text{Ir}_{45}\text{Co}_{55}$ samples still presented a comparable H_{upd} area to the $\text{Ir}_{28}\text{Co}_{72}$ series, indicating that the sample was not completely oxidized. Nevertheless, the overpotential still decreased by about 10 mV after activation as in the case of the Co-rich samples due to the oxidation of the metallic surface (Fig. 4e). As a result, the activity measured after activation at 30 °C and 1.50 V_{RHE} increased to 57.6 $\text{Ag}^{-1}_{\text{Ir}}$, four times greater than the value of the commercial sample (Table 3). Still, it was approximately two times lower than the Ir-rich ($\text{Ir}_{28}\text{Co}_{72}$) samples under the same conditions. OER activity measured at 60 °C was nearly doubled from the previous step, i.e., 91.8 $\text{Ag}^{-1}_{\text{Ir}}$ at 1.46 V_{RHE} . The sharp activity increase reinforces the hypothesis that the samples only experience full activation during the protocol at high temperatures. Even at the start of this step the overpotential already decreased by 45 mV compared to the activity recorded after activation (Fig. S13). Since the reversible reduction in the overpotential due to temperature increase is approximately 25 mV, the further decrease supports the argument of a dynamic activation process. Additionally, the Tafel slope also decreased from 64 to 52 mV dec^{-1} between the activation and high-temperature OER respectively. The Ir-rich $\text{Ir}_{75}\text{Co}_{25}$ series exhibited the lowest values for the surface area and activity throughout the OER measurements. After acid leaching, the ECSA was determined to be $21.4 \pm 2.0 \text{ m}^2\text{g}^{-1}$, see Table 3. This is in good agreement with the observed top-down

morphology from the leached sample at the SEM (Fig. 2f), which featured the smallest clusters in all three series. The reduction in overpotential after activation was also minimal, i.e., ca. 3 mV (Fig. S13). The OER activity after activation at 30 °C was 44.3 $\text{Ag}^{-1}_{\text{Ir}}$ at 1.50 V_{RHE} , which is approximately 30 mV lower than that of the commercial benchmark under the same conditions. As also observed for the other IrCo series, the mass activity improved at 60 °C, reaching 62.7 $\text{Ag}^{-1}_{\text{Ir}}$ at 1.46 V_{RHE} as compared to the 10.14 $\text{Ag}^{-1}_{\text{Ir}}$ of the commercial benchmark. Interestingly, even though the mass activity results were at the lowest of the series in absolute numbers, a similar reduction in overpotential at high temperatures was observed as compared to $\text{Ir}_{45}\text{Co}_{55}$. (Fig. S13). The Tafel slope was the highest of the series and only decreased from 68 to 58 mV dec^{-1} between activation and high-temperature OER respectively, which was the smallest change in all series (see Table 3). Along the series, the ECSA, the Tafel and the mass activity followed the trend defined by the initial as-deposited Co content $\text{Ir}_{28}\text{Co}_{72} > \text{Ir}_{45}\text{Co}_{55} > \text{Ir}_{75}\text{Co}_{25}$. When combined with the catalyst morphology, this trend strongly suggests that a high initial Co content increases the catalyst utilization by increasing the ECSA in a dynamic process as the catalyst is activated. On the other hand, the specific activity was found to correlate with the XAS results and the Co content after leaching from the EDX results, which hints at a positive influence from the remaining Co in the structure. A summary of the main electrochemical results can be found in Table 3 below.

Some additional factors need to be considered together with the electrochemical results. As mentioned in the methods section, the deposition time for the magnetron targets was defined between 1 s and 6 s for Co and kept constant at 3 s for Ir in each cycle. The Ir loading calibration was performed in a continuous deposition of 1200 s. In a preliminary test, it was confirmed for Ir that the loading for the continuous deposition matched the loading for the cycled deposition by mass gravimetry. However, when measuring the expected ratios by EDX they were found to be different from the nominal. While EDX is a versatile tool to determine the spatial resolution of the thin catalyst layer and the element distribution on the substrate, it is known that absolute quantification using automatic standardless EDX profiles is generally poor [60]. We found that using 15 kV for the analysis was a compromise between good surface sensitivity and exciting the higher energy lines for better elemental analysis (Co K_{α} = 6.924 keV, Ir L_{α} = 9.147 keV) to maximize the number of counts. However, in the acid-leaching process, the catalyst loading is further reduced which leads to larger errors in the elemental quantification. Hence, we assumed the initial loading was unchanged for the electrochemical mass activity results, while it is likely that both the surface area and the mass activity might be larger than what was measured. The quantification of the changes in the Ir loading during electrochemical measurements is not trivial. Unlike other PGM catalysts (Pt, Pd), iridium is known to fully dissolve only in extremely aggressive conditions requiring high temperatures, pressures, and strong acids [61,62]. Therefore, the preparation of the samples for conventional ex-situ techniques such as Inductively Coupled Plasma Mass Spectrometry (ICP-MS) that relies on the analysis of the dissolved species is non-standard and complex. However, in recent years, some approaches have been taken to quantify the Ir loading or loss during the electrochemical measurements. One of the most relevant methods is the Scanning Flow Cell (SFC) coupled with an ICP-MS system, which allows to perform time-resolved measurements of the material loss during an electrochemical protocol. Unfortunately, it also does not provide information about the remaining catalyst in the deposited layer [63]. Furthermore, there is not yet a compatible design to combine the high-current capabilities of the GDE method with the access to analytics of the SFC ICP-MS. Additionally, most techniques have been optimized so far for the study of supported catalysts with Ir nanoparticles which are known to present higher degradation rates compared to self-supported catalysts [11,34,35]. Since the purpose of this study was to assess the performance of different Ir-based catalysts under the same conditions and using a comparative approach, a quantitative study of the Ir loading

loss or the formation of transient species was not performed. In addition, speculations about specific activity changes in correlation to XAS data were made with data measured at 30 °C in combination with the ECSA measurement in metallic state by Hupd. However, the increase in the double layer capacity of the CVs due to the oxidation to IrOx after the OER at higher temperatures (see Fig. 2f) would have resulted in different surface areas and thus different specific activities. Therefore the specific activity reported at 60 °C has to be taken with caution. Other in-situ methods such as the mercury underpotential deposition could have also been considered [64]. However, this was not possible, as the membrane would need to be removed to avoid poisoning, impeding further electrochemistry. For the same reason, most material characterization methods in this study have been limited to the after-leaching state. Further insight into the dynamic catalyst activation at high temperatures and its link to the morphology may be achieved with *in-operando* XAS methods as soon as they are developed. Nevertheless, these limitations were considered as boundary conditions to help the discussion and understanding of our results.

4. Conclusion

In this study, we applied the GDE method to perform activity measurements of PVD-produced catalysts for the OER. First, three series of Ir–Co catalysts with equal 250 µg/cm² Ir loading were sputtered on carbon substrate using different Co:Ir weight ratios (Ir₂₈Co₇₂, Ir₄₅Co₅₅, Ir₇₅Co₂₅). To create a self-supported nanoporous structure with increased ECSA, Co was removed in an acid-leaching step. This is rendering a distinct dendrital surface morphology with Ir-rich clusters and slight changes in crystallinity. During the process, a mixed metallic and oxide structure with local Ir–Co coordination is formed. A higher initial Co content leads to larger surface areas after leaching, outperforming the OER activity of a commercial IrOx catalyst benchmarked at 30 °C and 60 °C. Overall, the performance followed the Co:Ir series Ir₂₈Co₇₂ > Ir₄₅Co₅₅ > Ir₇₅Co₂₅ > IrOx, where the best-performing catalyst at 60 °C reached more than a tenth-fold increase in mass activity over the commercial sample. The performance increase as compared to the benchmark catalyst, accounting for loading and preparation differences, can be due to higher dispersion in addition to a ligand effect. The latter is supported by the specific activity trend correlation with the remaining Co after acid leaching and XAS coordination data. A strain effect, by comparison, was not supported by the XAS data. The temperature increase and dynamic surface activation due to oxidation of metallic Ir, both observed by CV and the OER activity, had a positive influence on the catalyst activity. The authors acknowledge that the complex mechanisms behind the influence of the Co content and the electrochemical performance may not be fully explained from the measurement results, but also remain beyond the scope of this study. On the other hand, it was demonstrated that the flexible and reproducible characteristics achievable from the nanostructured PVD-produced catalysts in combination with the three-electrode GDE setup can reveal further insights into the electrode evolution under more realistic conditions than traditional methods such as RDE, helping to fast-track OER catalyst experimental research.

CRedit authorship contribution statement

Pablo Collantes Jiménez: Methodology, Investigation, Writing – original draft. **Gustav Sievers:** Writing – review & editing, Supervision, Conceptualization. **Antje Quade:** Investigation, Methodology. **Volker Brüser:** Supervision, Methodology. **Rebecca Katharina Pittkowski:** Investigation, Methodology. **Matthias Arenz:** Writing – review & editing, Supervision, Conceptualization, All authors checked and approved the final version of the manuscript.

Declaration of competing interest

The authors declare the following financial interests/personal relationships which may be considered as potential competing interests: Gustav Sievers has patent #DE102016013185B4.

Data availability

Data will be made available on request.

Acknowledgements

The authors gratefully acknowledge the financial support by the German Federal Ministry of Education and Research (BMBF) in the framework of the VIP + Projekt. 03VP06451 (3DNanoMe). The authors thank Adam Clark from the SuperXAS beamline X10DA at the Paul Scherrer Institute (PSI) for measuring the XAS data via mail-in service. MA and RKP acknowledge funding from the Swiss National Science Foundation (SNSF) via project No. 200021 184742 and the Danish National Research Foundation Center for High Entropy Alloys Catalysis (CHEAC) DNRF-149.

Appendix A. Supplementary data

Supplementary data to this article can be found online at <https://doi.org/10.1016/j.jpowsour.2023.232990>.

References

- [1] R. Ma, B. Cui, D. Hu, S.M. El-Bahy, Y. Wang, I.H.E. Azab, A.Y. Elnaggar, H. Gu, G.A. M. Mersal, M. Huang, V. Murugadoss, Enhanced energy storage of lead-free mixed oxide core double-shell barium strontium zirconate titanate@magnesium aluminate/zinc oxide-boron trioxide-silica ceramic nanocomposites, *Adv. Compos. Hybrid Mater.* 5 (2022) 1477–1489, <https://doi.org/10.1007/s42114-022-00509-z>.
- [2] Y. Zhao, F. Liu, K. Zhu, S. Maganti, Z. Zhao, P. Bai, Three-dimensional printing of the copper sulfate hybrid composites for supercapacitor electrodes with ultra-high areal and volumetric capacitances, *Adv. Compos. Hybrid Mater.* 5 (2022) 1537–1547, <https://doi.org/10.1007/s42114-022-00430-5>.
- [3] Y. Zhang, L. Liu, L. Zhao, C. Hou, M. Huang, H. Algadi, D. Li, Q. Xia, J. Wang, Z. Zhou, X. Han, Y. Long, Y. Li, Z. Zhang, Y. Liu, Sandwich-like CoMoP₂/MoP heterostructures coupling N, P co-doped carbon nanosheets as advanced anodes for high-performance lithium-ion batteries, *Adv. Compos. Hybrid Mater.* 5 (2022) 2601–2610, <https://doi.org/10.1007/s42114-022-00535-x>.
- [4] Y. Ma, X. Xie, W. Yang, Z. Yu, X. Sun, Y. Zhang, X. Yang, H. Kimura, C. Hou, Z. Guo, W. Du, Recent advances in transition metal oxides with different dimensions as electrodes for high-performance supercapacitors, *Adv. Compos. Hybrid Mater.* 4 (2021) 906–924, <https://doi.org/10.1007/s42114-021-00358-2>.
- [5] C. Dang, Q. Mu, X. Xie, X. Sun, X. Yang, Y. Zhang, S. Maganti, M. Huang, Q. Jiang, I. Seok, W. Du, C. Hou, Recent progress in cathode catalyst for nonaqueous lithium oxygen batteries: a review, *Adv. Compos. Hybrid Mater.* 5 (2022) 606–626, <https://doi.org/10.1007/s42114-022-00500-8>.
- [6] S.C. D'Angelo, S. Cobo, V. Tulus, A. Nabera, A.J. Martín, J. Pérez-Ramírez, G. Guillén-Gosálbez, Planetary boundaries analysis of low-carbon ammonia production routes, *ACS Sustain. Chem. Eng.* 9 (2021) 9740–9749, <https://doi.org/10.1021/acssuschemeng.1c01915>.
- [7] Net Zero by 2050 - A Roadmap for the Global Energy Sector, IEA, IEA, Paris, 2021. <https://www.iea.org/reports/net-zero-by-2050>.
- [8] IRENA, Green Hydrogen Cost Reduction, 2020 publications/2020/Dec/Green-hydrogen-cost-reduction%0Ahttps://www.irena.org/-/media/Files/IRENA/Agency/Publication/2020/Dec/IRENA_Green_hydrogen_cost_2020.pdf.
- [9] S.M. Saba, M. Müller, M. Robinus, D. Stolten, The investment costs of electrolysis – a comparison of cost studies from the past 30 years, *Int. J. Hydrogen Energy* 43 (2018) 1209–1223, <https://doi.org/10.1016/j.ijhydene.2017.11.115>.
- [10] M. Carmo, D.L. Fritz, J. Mergel, D. Stolten, A comprehensive review on PEM water electrolysis, *Int. J. Hydrogen Energy* 38 (2013) 4901–4934, <https://doi.org/10.1016/j.ijhydene.2013.01.151>.
- [11] A.W. Jensen, G.W. Sievers, K.D. Jensen, J. Quinson, J.A. Arminio-Ravelo, V. Brüser, M. Arenz, M. Escudero-Escribano, Self-supported nanostructured iridium-based networks as highly active electrocatalysts for oxygen evolution in acidic media, *J. Mater. Chem. A Mater* 8 (2020) 1066–1071, <https://doi.org/10.1039/c9ta12796h>.
- [12] C. Wei, R.R. Rao, J. Peng, B. Huang, I.E.L. Stephens, M. Risch, Z.J. Xu, Y. Shao-Horn, Recommended practices and benchmark activity for hydrogen and oxygen electrocatalysis in water splitting and fuel cells, *Adv. Mater.* 31 (2019), 1806296, <https://doi.org/10.1002/adma.201806296>.

- [13] Johnson Matthey 2022, No Title, PGM Management, 2022. June 28, 2022), <https://matthey.com/products-and-markets/pgms-and-circularity/pgm-management>
- [14] M. Egi, C. Shi, J. Xie, F. Kang, H. Qi, X. Tan, Z. Huang, J. Liu, J. Guo, Synergetic effect of Ni-Au bimetal nanoparticles on urchin-like TiO₂ for hydrogen and arabinose co-production by glucose photoreforming, *Adv. Compos. Hybrid Mater.* 6 (2023) 1–14, <https://doi.org/10.1007/s42114-022-00580-6>.
- [15] A.L. Strickler, R.A. Flores, L.A. King, J.K. Norskov, M. Bajdich, T.F. Jaramillo, Systematic investigation of iridium-based bimetallic thin film catalysts for the oxygen evolution reaction in acidic media, *ACS Appl. Mater. Interfaces* 11 (2019) 34059–34066, <https://doi.org/10.1021/acsami.9b13697>.
- [16] X. Chen, M. Xu, S. Li, C. Li, X. Sun, S. Mu, J. Yu, Ultrafine IrNi bimetallics encapsulated in zeolitic imidazolate frameworks-derived porous N-doped carbon for boosting oxygen evolution in both alkaline and acidic electrolytes, *Adv. Mater. Interfac.* 7 (2020) 1–8, <https://doi.org/10.1002/admi.202001145>.
- [17] S.L. Hamukwaya, Z. Zhao, H. Hao, H.M. Abo-Dief, K.M. Abualnaja, A.K. Alanazi, M.M. Mashigaidze, S.M. El-Bahy, M. Huang, Z. Guo, Enhanced photocatalytic performance for hydrogen production and carbon dioxide reduction by a mesoporous single-crystal-like TiO₂ composite catalyst, *Adv. Compos. Hybrid Mater.* 5 (2022) 2620–2630, <https://doi.org/10.1007/s42114-022-00545-9>.
- [18] B.M. Tackett, W. Sheng, S. Kattel, S. Yao, B. Yan, K.A. Kuttiyiel, Q. Wu, J.G. Chen, Reducing iridium loading in oxygen evolution reaction electrocatalysts using core-shell particles with nitride cores, *ACS Catal.* 8 (2018) 2615–2621, <https://doi.org/10.1021/acscatal.7b04410>.
- [19] Y.T. Kim, P.P. Lopes, S.A. Park, A.Y. Lee, J. Lim, H. Lee, S. Back, Y. Jung, N. Danilovic, V. Stamenkovic, J. Erlebacher, J. Snyder, N.M. Markovic, Balancing activity, stability and conductivity of nanoporous core-shell iridium/iridium oxide oxygen evolution catalysts, *Nat. Commun.* 8 (2017) 1–8, <https://doi.org/10.1038/s41467-017-01734-7>.
- [20] C. van Pham, M. Bühler, J. Knöppel, M. Bierling, D. Seeberger, D. Escalera-López, K.J.J. Mayrhofer, S. Cherevko, S. Thiele, IrO₂ coated TiO₂ core-shell microparticles advance performance of low loading proton exchange membrane water electrolyzers, *Appl. Catal., B* 269 (2020), <https://doi.org/10.1016/j.apcatb.2020.118762>.
- [21] A. Ahmed, S. Seth, J. Purewal, A.G. Wong-Foy, M. Veenstra, A.J. Matzger, D. J. Siegel, Exceptional hydrogen storage achieved by screening nearly half a million metal-organic frameworks, *Nat. Commun.* 10 (2019), <https://doi.org/10.1038/s41467-019-09365-w>.
- [22] J. Gao, H. Tao, B. Liu, Progress of nonprecious-metal-based electrocatalysts for oxygen evolution in acidic media, *Adv. Mater.* 33 (2021) 1–18, <https://doi.org/10.1002/adma.202003786>.
- [23] E. Chamanehpour, M.H. Sayadi, M. Hajiani, A hierarchical graphitic carbon nitride supported by metal-organic framework and copper nanocomposite as a novel bifunctional catalyst with long-term stability for enhanced carbon dioxide photoreduction under solar light irradiation, *Adv. Compos. Hybrid Mater.* 5 (2022) 2461–2477, <https://doi.org/10.1007/s42114-022-00459-6>.
- [24] J. Zhao, K. Bao, M. Xie, D. Wei, K. Yang, X. Zhang, C. Zhang, Z. Wang, X. Yang, Two-dimensional ultrathin networked CoP derived from Co(OH)₂ as efficient electrocatalyst for hydrogen evolution, *Adv. Compos. Hybrid Mater.* 5 (2022) 2421–2428, <https://doi.org/10.1007/s42114-022-00455-w>.
- [25] J. Schröder, V.A. Mints, A. Bornet, E. Berner, M.F. Tovini, J. Quinson, G.K. H. Wiberg, F. Bizzotto, H.A. El-Sayed, M. Arenz, The gas diffusion electrode setup as straightforward testing device for proton exchange membrane water electrolyzer catalysts, *JACS Au* 1 (2021) 247–251, <https://doi.org/10.1021/JACS.AU.1C00015>.
- [26] G.W. Sievers, A.W. Jensen, V. Brüser, M. Arenz, M. Escudero-Escribano, Sputtered platinum thin-films for oxygen reduction in gas diffusion electrodes: a model system for studies under realistic reaction conditions, *Surfaces* 2 (2019) 336–348, <https://doi.org/10.3390/surfaces2020025>.
- [27] J. Du, J. Quinson, A. Zana, M. Arenz, Elucidating Pt-based nanocomposite catalysts for the oxygen reduction reaction in rotating disk electrode and gas diffusion electrode measurements, *ACS Catal.* 11 (2021) 7584–7594, <https://doi.org/10.1021/acscatal.1c01496>.
- [28] T. Tian, Y. Cheng, Z. Sun, K. Huang, M. Lei, H. Tang, Carbon nanotubes supported oxygen reduction reaction catalysts: role of inner tubes, *Adv. Compos. Hybrid Mater.* 6 (2023) 1–10, <https://doi.org/10.1007/s42114-022-00592-2>.
- [29] R. Wang, Z. Zhang, P. Du, Z. Fu, K. Huang, K. Xu, Y. Du, D. Fan, R. Zhang, M. Lei, Efficient synthesis of sulfur-modified cobalt hydroxide self-supported electrocatalysts for enhanced oxygen evolution, *Adv. Compos. Hybrid Mater.* 5 (2022) 2491–2499, <https://doi.org/10.1007/s42114-022-00495-2>.
- [30] Z. Zhao, Y. Lin, J. Wu, J. Li, M. Lei, Mixed-phase cobalt-based nanosheets prepared by rapid thermal annealing for oxygen evolution catalysis, *Adv. Compos. Hybrid Mater.* 5 (2022) 2589–2600, <https://doi.org/10.1007/s42114-022-00537-9>.
- [31] J. Liang, H. Shen, J. Kong, Steel mesh reinforced Ni(OH)₂ nanosheets with enhanced oxygen evolution reaction performance, *ES Materials and Manufacturing* 14 (2021) 79–86, <https://doi.org/10.30919/esmm5f454>.
- [32] D. Xue, J. Cheng, P. Yuan, B.A. Lu, H. Xia, C.C. Yang, C.L. Dong, H. Zhang, F. Shi, S. C. Mu, J.S. Hu, S.G. Sun, J.N. Zhang, Boron-tethering and regulative electronic states around iridium species for hydrogen evolution, *Adv. Funct. Mater.* 32 (2022) 1–9, <https://doi.org/10.1002/adfm.202113191>.
- [33] S.I. Nefedkin, M.A. Klimova, A.V. Ryabukhin, A.V. Chizhov, I.I. Levin, Fabrication of catalytic compositions for electrodes of fuel cells and water electrolyzers with proton-exchange membrane by magnetron sputtering of composite targets, *Nanobiotechnology Reports* 16 (2021) 516–524, <https://doi.org/10.1134/S2635167621040078>.
- [34] G.W. Sievers, J.R. Bowen, V. Brüser, M. Arenz, Support-free nanostructured Pt–Cu electrocatalyst for the oxygen reduction reaction prepared by alternating magnetron sputtering, *J. Power Sources* 413 (2019) 432–440, <https://doi.org/10.1016/j.jpowsour.2018.12.044>.
- [35] G.W. Sievers, A.W. Jensen, J. Quinson, A. Zana, F. Bizzotto, M. Oezaslan, A. Dworzak, J.K.K. Kirkensgaard, T.E.L. Smithuysen, S. Kadkhodazadeh, M. Juelsholt, K.M.Ø. Jensen, K. Anklam, H. Wan, J. Schäfer, K. Cépe, M. Escudero-Escribano, J. Rossmeisl, A. Quade, V. Brüser, M. Arenz, Self-supported Pt–CoO networks combining high specific activity with high surface area for oxygen reduction, *Nat. Mater.* 20 (2021) 208–213, <https://doi.org/10.1038/s41563-020-0775-8>.
- [36] B. Han, C.E. Carlton, A. Kongkanand, R.S. Kukreja, B.R. Theobald, L. Gan, R. O'Malley, P. Strasser, F.T. Wagner, Y. Shao-Horn, Record activity and stability of dealloyed bimetallic catalysts for proton exchange membrane fuel cells, *Energy Environ. Sci.* 8 (2014) 258–266, <https://doi.org/10.1039/C4EE02144D>.
- [37] J. Knöppel, M. Möckl, D. Escalera-López, K. Stojanovski, M. Bierling, T. Böhm, S. Thiele, M. Rzepka, S. Cherevko, On the limitations in assessing stability of oxygen evolution catalysts using aqueous model electrochemical cells, *Nat. Commun.* 12 (2021), <https://doi.org/10.1038/s41467-021-22296-9>.
- [38] S. Geiger, O. Kasian, M. Ledendecker, E. Pizzutillo, A.M. Mingers, W.T. Fu, O. Diaz-Morales, Z. Li, T. Oellers, L. Fruchter, A. Ludwig, K.J.J. Mayrhofer, M.T.M. Koper, S. Cherevko, The stability number as a metric for electrocatalyst stability benchmarking, *Nat Catal* 1 (2018) 508–515, <https://doi.org/10.1038/s41929-018-0085-6>.
- [39] T. Lazaridis, B.M. Stühmeier, H.A. Gasteiger, H.A. El-Sayed, Capabilities and limitations of rotating disk electrodes versus membrane electrode assemblies in the investigation of electrocatalysts, *Nat Catal* 5 (2022), <https://doi.org/10.1038/s41929-022-00776-5>.
- [40] H.A. El-Sayed, A. Weiß, L.F. Olbrich, G.P. Putro, H.A. Gasteiger, OER catalyst investigation using RDE technique: a stability measure or an artifact? *J. Electrochem. Soc.* 166 (2019) F458–F464, <https://doi.org/10.1149/2.0301908jes>.
- [41] M. Inaba, A.W. Jensen, G.W. Sievers, M. Escudero-Escribano, A. Zana, M. Arenz, Benchmarking high surface area electrocatalysts in a gas diffusion electrode: measurement of oxygen reduction activities under realistic conditions, *Energy Environ. Sci.* 11 (2018) 988–994, <https://doi.org/10.1039/c8ee00019k>.
- [42] K. Ehelebe, D. Seeberger, M.T.Y. Paul, S. Thiele, K.J.J. Mayrhofer, S. Cherevko, Evaluating electrocatalysts at relevant currents in a half-cell: the impact of Pt loading on oxygen reduction reaction, *J. Electrochem. Soc.* 166 (2019) F1259–F1268, <https://doi.org/10.1149/2.0911915jes>.
- [43] S. Nösberger, J. Du, J. Quinson, E. Berner, A. Zana, G.K.H. Wiberg, M. Arenz, The gas diffusion electrode setup as a testing platform for evaluating fuel cell catalysts: a comparative RDE-GDE study, *Electrochemical Science Advances* (2022) 1–12, <https://doi.org/10.1002/elsa.202100190>.
- [44] K. Ehelebe, N. Schmitt, G. Sievers, A.W. Jensen, A. Hrnjić, P. Collantes Jiménez, P. Kaiser, M. Geuß, Y.P. Ku, P. Jovanović, K.J.J. Mayrhofer, B. Etzold, N. Hodnik, M. Escudero-Escribano, M. Arenz, S. Cherevko, Benchmarking fuel cell electrocatalysts using gas diffusion electrodes: inter-lab comparison and best practices, *ACS Energy Lett.* 7 (2022) 816–826, <https://doi.org/10.1021/acseenergylett.1c02659>.
- [45] S.M. Alia, B. Rasimick, C. Ngo, K.C. Neyerlin, S.S. Kocha, S. Pylypenko, H. Xu, B. S. Pivovar, Activity and durability of iridium nanoparticles in the oxygen evolution reaction, *J. Electrochem. Soc.* 163 (2016), <https://doi.org/10.1149/2.0151611jes>.
- [46] J.B. Gerken, J.G. McAlpin, J.Y.C. Chen, M.L. Rigsby, W.H. Casey, R.D. Britt, S. Stahl, Electrochemical water oxidation with cobalt-based electrocatalysts from pH 0–14: the thermodynamic basis for catalyst structure, stability, and activity, *J. Am. Chem. Soc.* 133 (2011) 14431–14442, <https://doi.org/10.1021/ja205647m>.
- [47] A.W. Grant, Cobalt complexes and le Chatelier, *J. Chem. Educ.* 61 (1984) 466, <https://doi.org/10.1021/ed061p466>.
- [48] V.R. Stamenkovic, B.S. Mun, M. Arenz, K.J.J. Mayrhofer, C.A. Lucas, G. Wang, P. N. Ross, N.M. Markovic, Trends in electrocatalysis on extended and nanoscale Pt-bimetallic alloy surfaces, *Nat. Mater.* 6 (2007) 241–247, <https://doi.org/10.1038/nmat1840>.
- [49] E. Slavcheva, I. Radev, S. Bliznakov, G. Topalov, P. Andreev, E. Budevski, Sputtered iridium oxide films as electrocatalysts for water splitting via PEM electrolysis, *Electrochim. Acta* 52 (2007) 3889–3894, <https://doi.org/10.1016/j.electacta.2006.11.005>.
- [50] P. Kús, A. Ostroverkh, I. Khalakhan, R. Fiala, Y. Kosto, B. Šmíd, Y. Lobko, Y. Yakovlev, J. Nováková, I. Matolínová, V. Matolín, Magnetron sputtered thin-film vertically segmented Pt–Ir catalyst supported on TiC for anode side of proton exchange membrane unitized regenerative fuel cells, *Int. J. Hydrogen Energy* 44 (2019) 16087–16098, <https://doi.org/10.1016/j.ijhydene.2019.04.216>.
- [51] W. Hu, H. Zhong, W. Liang, S. Chen, Ir-surface enriched porous Ir–Co oxide hierarchical architecture for high performance water oxidation in acidic media, *ACS Appl. Mater. Interfaces* 6 (2014) 12729–12736, <https://doi.org/10.1021/am5027192>.
- [52] S. Chatterjee, S. Intikhab, L. Profit, Y. Li, F. Natu, R. Gawas, J. Snyder, Nanoporous multimetallic Ir alloys as efficient and stable electrocatalysts for acidic oxygen evolution reactions, *J. Catal.* 393 (2021) 303–312, <https://doi.org/10.3809/phys.1.2017.21>.
- [53] J. Erlebacher, M.J. Aziz, A. Karma, N. Dimitrov, K. Sieradzki, Evolution of nanoporosity in dealloying, *Nature* 410 (2001) 450–453, <https://doi.org/10.1038/35068529>.
- [54] S. Parida, D. Kramer, C.A. Volkert, H. Rösner, J. Erlebacher, J. Weissmüller, Volume change during the formation of nanoporous gold by dealloying, *Phys. Rev. Lett.* 97 (2006) 4–7, <https://doi.org/10.1103/PhysRevLett.97.035504>.

- [55] S. Koh, P. Strasser, Electrocatalysis on bimetallic surfaces: modifying catalytic reactivity for oxygen reduction by voltammetric surface dealloying, *J. Am. Chem. Soc.* 129 (2007) 12624–12625, <https://doi.org/10.1021/ja0742784>.
- [56] B. Han, C.E. Carlton, A. Kongkanand, R.S. Kukreja, B.R. Theobald, L. Gan, R. O'Malley, P. Strasser, F.T. Wagner, Y. Shao-Horn, Record activity and stability of dealloyed bimetallic catalysts for proton exchange membrane fuel cells, *Energy Environ. Sci.* 8 (2015) 258–266, <https://doi.org/10.1039/C4EE02144D>.
- [57] M. Gößler, E. Hengge, M. Bogar, M. Albu, D. Knez, H. Amenitsch, R. Würschum, In situ study of nanoporosity evolution during dealloying AgAu and CoPd by grazing-incidence small-angle X-ray scattering, *J. Phys. Chem. C* 126 (2022) 4037–4047, <https://doi.org/10.1021/acs.jpcc.1c09592>.
- [58] C. Wei, S. Sun, D. Mandler, X. Wang, S.Z. Qiao, Z.J. Xu, Approaches for measuring the surface areas of metal oxide electrocatalysts for determining their intrinsic electrocatalytic activity, *Chem. Soc. Rev.* 48 (2019) 2518–2534, <https://doi.org/10.1039/c8cs00848e>.
- [59] T. Shinagawa, A.T. Garcia-Esparza, K. Takanabe, Insight on Tafel slopes from a microkinetic analysis of aqueous electrocatalysis for energy conversion, *Sci. Rep.* 5 (2015) 1–21, <https://doi.org/10.1038/srep13801>.
- [60] D.E. Newbury, N.W.M. Ritchie, Is scanning electron microscopy/energy dispersive X-ray spectrometry (SEM/EDS) quantitative? *Scanning* 35 (2013) 141–168, <https://doi.org/10.1002/SCA.21041>.
- [61] A.P.J. Hodgson, K.E. Jarvis, R.W. Grimes, O.J. Marsden, Development of an iridium dissolution method for the evaluation of potential radiological device materials, *J. Radioanal. Nucl. Chem.* 307 (2015) 2181–2186, <https://doi.org/10.1007/S10967-015-4381-1>, 3. 307 (2015).
- [62] M.M. Todand, I. JarviS, K.E. Jarvis, Microwave digestion and alkali fusion procedures for the determination of the platinum-group elements and gold in geological materials by ICP-MS, *Chem. Geol.* 124 (1995) 21–36, [https://doi.org/10.1016/0009-2541\(95\)00021-D](https://doi.org/10.1016/0009-2541(95)00021-D).
- [63] J.P. Grote, A.R. Zeradjanin, S. Cherevko, K.J.J. Mayrhofer, Coupling of a scanning flow cell with online electrochemical mass spectrometry for screening of reaction selectivity, *Rev. Sci. Instrum.* 85 (2014), <https://doi.org/10.1063/1.4896755>.
- [64] S. Duran, M. Elmaalouf, M. Odziomek, J.Y. Piquemal, M. Faustini, M. Giraud, J. Peron, C. Tard, Electrochemical active surface area determination of iridium-based mixed oxides by mercury underpotential deposition, *Chemelectrochem* 8 (2021) 3519–3524, <https://doi.org/10.1002/celec.202100649>.